

Staining and embedding the whole mouse brain for electron microscopy

Shawn Mikula, Jonas Binding & Winfried Denk

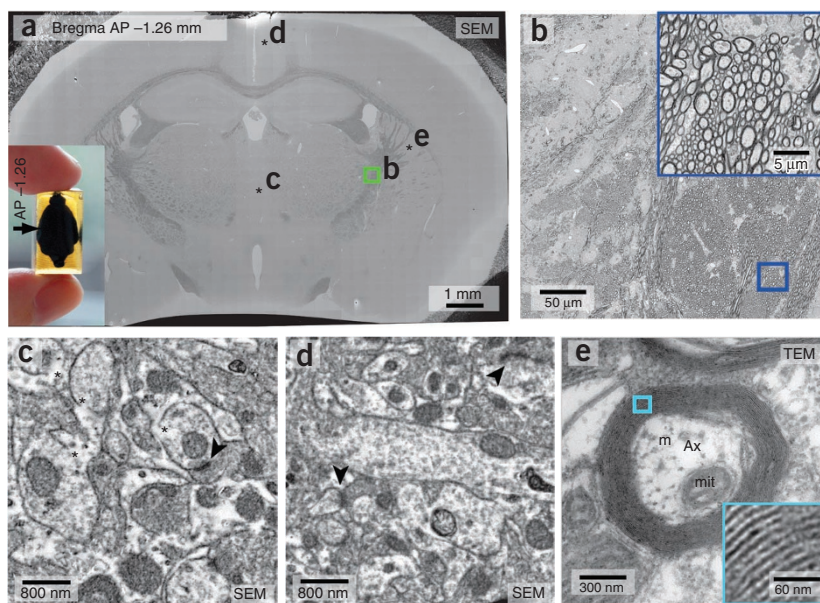
The development of methods for imaging large contiguous volumes with the electron microscope could allow the complete mapping of a whole mouse brain at the single-axon level. We developed a method based on prolonged immersion that enables staining and embedding of the entire mouse brain with uniform myelin staining and a moderate preservation of the tissue's ultrastructure. We tested the ability to follow myelinated axons using serial block-face electron microscopy.

Mapping the mouse inter-areal connectome, also called the projectome¹ because it contains all projections between areas, would profoundly advance our understanding of whole-brain function by showing precise pathways of information flow. Currently, the most comprehensive map is only 10% complete and is based on a meta-analysis of the rodent connectivity literature², mostly tracer injection studies. Local injection-based analysis can be very

sensitive, but mapping all connections requires probing each of the approximately 1,000 brain areas multiple times. Thus, an estimated 10,000 brains² would need to be injected, imaged, aligned to a common reference and analyzed. Alternatively, one could image a single brain at a resolution sufficient to trace all axons at once. The set of all axonal trajectories would then comprise a map of all inter-areal connections. Currently only electron microscopy provides sufficient resolution to follow individual axons reliably in densely stained samples. Following neural processes throughout a whole brain requires special sample preparation techniques that allow the entire brain to be fixed, stained and embedded.

There are two broad strategies for whole-brain staining: perfusion and immersion. In the first case, the animal's vasculature, from which no part of the brain is generally farther than a few tens of micrometers (ref. 3), is used to introduce fixation and staining chemicals into the tissue. Transcardial perfusion has long been the method of choice for the initial fixation of whole brains⁴. Perfusion of staining solutions has rarely been used, even though fixation and staining can be achieved^{5,6} using perfusion with osmium tetroxide (OsO₄), commonly used in the past as the sole fixative before aldehyde fixation⁴ was introduced. However, OsO₄ alone gives relatively poor membrane contrast^{4,7}, and OsO₄ perfusion results in incomplete and capricious staining of white matter^{5,6}, a serious problem if long-range axons are to be traced. The other way to introduce chemicals into tissue is by immersion, which relies on diffusion to transport the molecules from

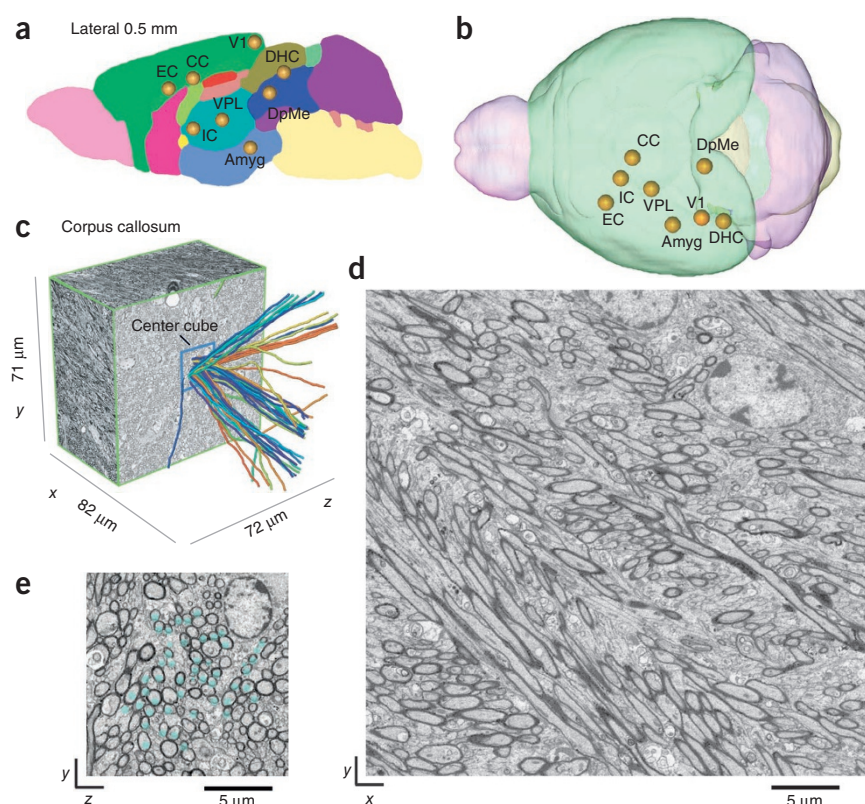
Figure 1 | Whole mouse brain stained with wbPATCO and embedded with Quetol. **(a)** Block-face image of a whole-brain cross-section cut at the level of bregma -1.26, coated with 5 nm platinum-carbon and imaged with scanning electron microscopy (SEM) using secondary-electron detection. Inset, horizontal view of the entire mouse brain after embedding; block dimensions are 6 × 8.5 × 14 mm³. AP, anterior-posterior. **(b)** Single image tile (green box in **a**). Inset, magnified subregion indicated by the blue box. **(c,d)** High-magnification SEM images from labeled asterisks of the block face in **a**, demonstrating ultrastructural preservation of deep **(c)** and superficial **(d)** regions. Note membrane discontinuities (asterisks) and postsynaptic densities (arrowheads). **(e)** High-magnification transmission electron microscopy (TEM) image of a 70-nm section taken from a region in the dorsolateral striatum (labeled asterisk in **a**) in a different sample. Note the intra-period and major dense lines in the inset in **e**. mit, mitochondrion; Ax, axon; m, microtubules.



Max-Planck Institute for Medical Research, Heidelberg, Germany. Correspondence should be addressed to S.M. (Shawn.Mikula@mpimf-heidelberg.mpg.de) or W.D. (Winfried.Denk@mpimf-heidelberg.mpg.de).

RECEIVED 14 MAY; ACCEPTED 28 SEPTEMBER; PUBLISHED ONLINE 21 OCTOBER 2012; DOI:10.1038/NMETH.2213

Figure 2 | Traceability analysis of eight regions of interest (ROIs) in the mouse brain. (a) Parasagittal view showing projections of ROIs. (b) Horizontal view of ROIs through a transparent brain. (c) Serial block-face electron microscopy stack from the corpus callosum, cut down the middle, with 50 traced axons emerging, randomly colored. (d) Single *xy* image from the stack. (e) *yz* reslice from the center of a cube (same as in c) showing locations of the 50 seed tracings (cyan points) for the axons shown in c. Amyg, amygdala; CC, corpus callosum; DHC, dorsal hippocampal commissure; DpMe, deep mesencephalic nucleus; EC, external capsule; IC, internal capsule; V1, primary visual cortex (superficial layers); VPL, ventroposterolateral nucleus of the dorsal thalamus. Color coding in a and b denotes major brain subdivisions (cerebral cortex, olfactory bulb, cerebellum, brainstem, superior colliculus and so on).



the sample's surface to its interior. This approach, which has been used to stain and embed whole mouse brains for light-microscopic observation^{8,9}, scales unfavorably with sample size because diffusion times increase quadratically with distance^{10,11}. The brain is, therefore, commonly cut into pieces at most a few millimeters in size after the initial perfusion fixation^{12,13}. For whole-brain connectivity analysis, this is unsuitable because such cutting always leads to surface damage, which in all likelihood precludes the reliable tracing of thin axons from one piece to the adjacent one. Here we report a procedure that is based mostly on long immersion steps and results in whole-brain samples that are stained and embedded well enough to reliably follow myelinated axons.

Aside from the initial transcatheter perfusion, we based our approach on sample immersion. To compensate for the about tenfold increase in diffusion distance due to the larger size of a whole-brain sample, we increased the periods of immersion to 48 h for each staining step (**Supplementary Protocol**). Because the effective diffusion constants of the staining chemicals in brain tissue cannot be larger than that for small solutes in aqueous solutions, roughly $10^{-9} \text{ m}^2 \text{ s}^{-1}$ (ref. 14), diffusion cannot equilibrate concentrations over a distance of much more than 10 mm in 48 h (the whole adult mouse brain is less than 10 mm in width and height).

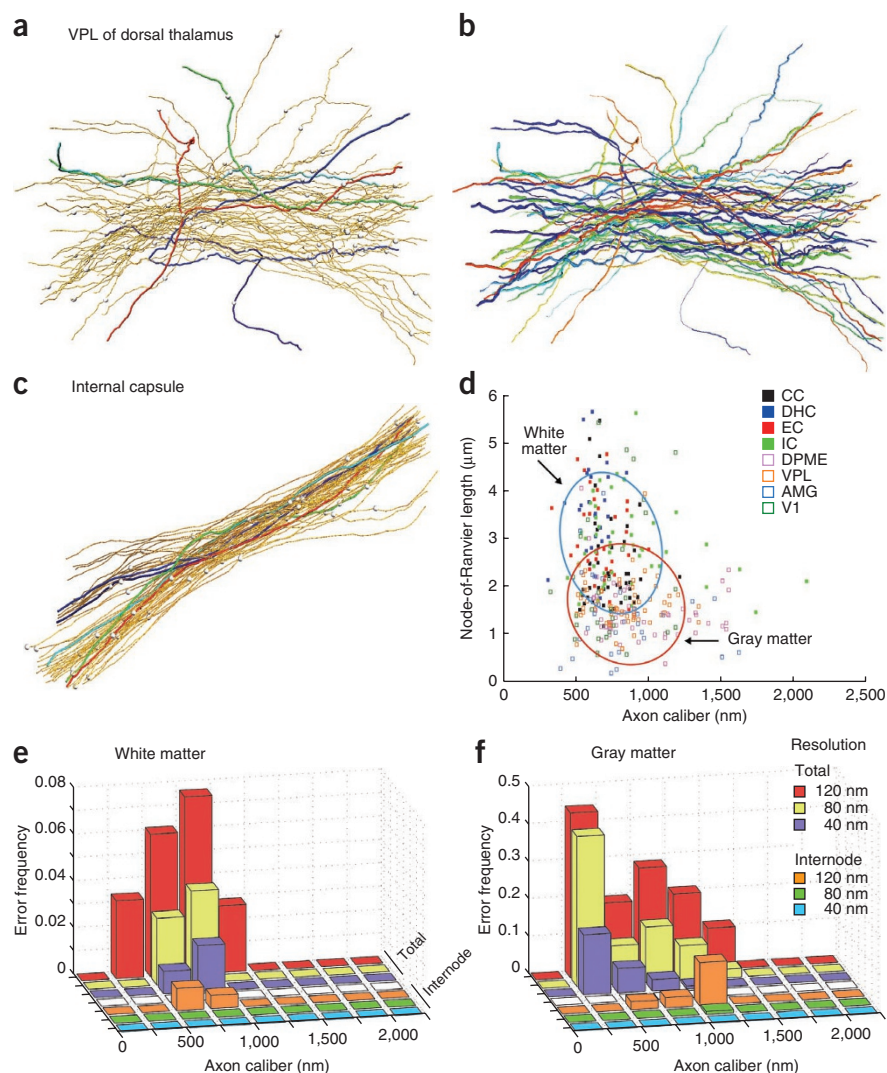
We initially used single-step incubations of brain hemispheres in OsO_4 (0.5–4%), using unbuffered and buffered (phosphate, Tris, cacodylate or collidine) solutions. None of the buffers improved penetration compared to the unbuffered case. When using unbuffered 2% OsO_4 at 20 °C, the penetration depths at different incubation times (data not shown) were consistent with an effective diffusion constant of roughly $2 \times 10^{-10} \text{ m}^2 \text{ s}^{-1}$, slower than free diffusion in water but much faster than the value of roughly $10^{-11} \text{ m}^2 \text{ s}^{-1}$ reported for liver¹⁰. Provided that the quantity of OsO_4 was sufficiently high (>250 mg) and the incubation times sufficiently long (>24 h), staining was uniform throughout the whole hemisphere, but the contrast was generally poor for membranes and myelin (**Supplementary Fig. 1a**). A further increase in incubation

time (>96 h) caused a decrease in membrane contrast. The inclusion of organic solvents did not facilitate penetration and led to a precipitation and progressive darkening of the staining solutions, presumably by reducing OsO_4 (ref. 15).

To improve contrast, we examined enhanced staining protocols, first using small tissue pieces (<1 mm) and short incubation times (90 min). Guided by the results, we then used hemispheres or whole brains and long incubation times (24–48 h). The protocols and comparative results are given in **Supplementary Tables 1 and 2**. By combining a single OsO_4 step with subsequent enhancement using uranyl acetate or lead aspartate, we slightly increased membrane contrast (**Supplementary Fig. 1b**). The OsO_4 -thiocarbohydrazide- OsO_4 (OTO) method⁷ yielded samples with high membrane contrast at short incubation times, but with incubation times of 24–48 h it suffered from cytosol darkening (**Supplementary Fig. 1c**), which reduced membrane contrast, masked synapses and resulted in bubble formation, possibly due to N_2 gas liberated from hydrazino groups in tissue-bound thiocarbohydrazide (TCH)¹⁶. The rOTO method, which uses ferrocyanide- OsO_4 ('reduced osmium'; refs. 17,18) instead of OsO_4 alone in the first incubation step, substantially increased membrane contrast over the OTO method, but stain penetration was poor even at 48-h incubation time, and the tissue ultrastructure was damaged (data not shown). By embedding and imaging samples at various points of the staining protocol, we determined that the poor penetration resulted from the reduced-osmium step.

Because the OTO method, despite suffering from nonuniform staining and embedding problems, resulted in good membrane contrast for short incubation times, we examined similar staining methods that also use TCH¹⁹. The periodic-acid-thiocarbohydrazide- OsO_4 (PATCO)¹⁹ method is a precursor of

Figure 3 | Analysis of axon morphological diversity and tracing error rate. (a–c) Axons traced in the ventroposterolateral nucleus (VPL) of the dorsal thalamus (a) with corresponding volumetric representation (b), and axons traced in the internal capsule (c). Fifty axons are displayed per region, with five axons highlighted in different colors to emphasize individual axon morphologies in relation to axon bundles and groupings (a,c). Nodes of Ranvier are indicated by small gray spheres. (d) Quantification of node-of-Ranvier length versus axon caliber in all eight regions of interest for axons containing a node of Ranvier with matching paranodes contained in the serial block-face electron microscopy cube. Ellipses indicate the s.d. of the data ($n = 339$ axons) for white- and gray-matter regions. (e,f) White-matter (e) and gray-matter (f) tracing error rates for myelinated axons of different axon-diameter bands and data display resolutions ($n = 200$ axons for each plot).



the OTO method but uses periodic acid instead of OsO_4 in the first incubation step and was originally designed to stain glycogen and other polysaccharides. We found that it also enhanced myelin contrast at least twofold (**Supplementary Fig. 1d**), possibly because of the high levels of glycolipids and cerebroside in myelin²⁰. By using buffered periodic-acid and TCH solutions, we obtained uniform and complete staining throughout the brain. We will use 'wbPATCO' to refer to the PATCO method that we optimized for whole-brain staining.

For embedding, we first tested an Epon 812 substitute, glycid ether 100 (Serva), and we found that it became viscous within several hours, thereby preventing complete infiltration. We next explored the use of low-viscosity epoxies and found that, with an immersion time of 12 h for each dehydration and epoxy-monomer infiltration step, both Spurr's resin²¹ and Quetol²² yielded whole-brain blocks of uniform mechanical quality. Image contrast did not depend on the embedding medium. Embedded samples were about 3–4% larger (in length) than they were following fixation.

Staining quality and uniformity were assessed for three brains prepared using the wbPATCO method. We acquired a set of block-face images at 80-nm pixel size that covered an entire coronal cross-section through one whole-brain sample (WB1405, **Fig. 1**). Upon close inspection of the individual image tiles (**Fig. 1b**), we observed that staining and tissue preservation were uniform across the entire cross-section. Ultrastructural preservation was moderately good and consistent in deep and superficial regions of the sample (**Fig. 1**).

To analyze traceability of myelinated axons in wbPATCO samples, we acquired serial block-face electron microscopy (SBEM) stacks from several locations distributed widely throughout the brain (**Fig. 2a,b**). No cutting problems were apparent (**Fig. 2c–e** and **Supplementary Video 1**), thus indicating

that epoxy infiltration and polymerization were complete throughout the sample. To determine axon traceability as a function of imaging resolution, we traced the SBEM stacks at the native 40-nm voxel size and down-sampled to 80-nm and 120-nm resolution (**Figs. 2c** and **3**).

Axons were generally straight and followed a dominant direction in white matter, but they followed more tortuous paths with no apparent direction preference in gray matter (**Fig. 3a–c** and **Supplementary Video 2**). On average, there were 0.92 nodes on each of the traced white-matter axons (10.14 nodes per mm, $n = 200$ axons), with no correlation apparent in node locations for neighboring axons. For gray matter, the number of nodes was slightly larger (1.21 nodes per axon traced, 11.58 nodes per mm, $n = 200$ axons), presumably because of the higher rate of branching. Although the distributions of axon calibers did not vary substantially among regions of interest, the node-of-Ranvier lengths showed more variation, ranging from 1 to 4 μm (**Fig. 3d**). For example, node-of-Ranvier length in the amygdala was $1.39 \pm 0.84 \mu\text{m}$ (\pm s.d., $n = 30$), whereas in the dorsal hippocampal commissure it was $3.54 \pm 0.91 \mu\text{m}$ ($n = 27$). We found a mean inner-axon caliber of 873 nm for white matter ($n = 200$ axons), which is substantially larger than the 510 nm reported for subcortical white matter²³

and 460 nm for the corpus callosum²⁴. This discrepancy far exceeds the overall linear expansion of 3–4% seen in our sample, but it is possible that axons shrank more in their preparation or expanded more in our preparation, or that the sampled areas were different.

Error rates for tracing differed for white and gray matter but did not depend much on axon diameter for axons with diameters greater than 500 nm (**Fig. 3e,f**). At the 40-nm native resolution, tracing errors were confined to nodes of Ranvier, with about one error for every 80 nodes (one error per 32 and 17 nodes at 80- and 120-nm resolution, respectively, $n = 200$ axons) in white matter and one error per 30 nodes (10 and 6 nodes at 80 and 120 nm, $n = 200$ axons) in gray matter (**Supplementary Table 3**). At 80-nm resolution, there were still no errors in internode segments for white matter, but one error occurred for every 100 mm of internode length in gray matter.

We have demonstrated that the whole mouse brain can be stained and embedded in a way that is suitable for ultramicrotomy and electron microscopic imaging. The contrast is uniform and sufficient for serial block-face imaging. Myelinated axons are traceable with low error rates. A further reduction in error rate is expected if a complete mutual assignment of paranodes is performed on the basis of their geometrical parameters, such as direction and diameter.

At similar axon calibers, white- and gray-matter error rates differ, possibly owing to differences in tortuosity: in gray matter, when encountering a node of Ranvier, the matching paranode cannot be found by simply continuing along the same direction.

The ultrastructure in our samples is preserved well enough to permit the recognition of unmyelinated processes and synapses; however, low membrane contrast and excessive cytosol staining prevent the reliable tracing of unmyelinated processes over long distances, making the wbPATCO method unsuitable for mapping complete neural circuits.

At this point it is unclear what fraction of the projectome can be recovered by following only myelinated axons because not all long-range axons are myelinated. The myelination of modulatory projections is sparse (or absent). Estimates from subcortical white matter in the adult mouse brain suggest that about a third of projection axons are myelinated²³. An open question is whether, aside from dopaminergic projections, there are areas that are connected by only unmyelinated fibers or whether all inter-areal connections contain a mixture of myelinated and unmyelinated fibers. If the latter is the case, a map of all myelinated axons in a single mouse brain would yield a relatively complete catalog of all inter-areal projections.

METHODS

Methods and any associated references are available in the [online version of the paper](#).

Note: Supplementary information is available in the [online version of the paper](#).

ACKNOWLEDGMENTS

We thank I. Sonntag and M. Helmstaedter for help with traceability analysis, S. Hillmer and U. Mersdorf for help with transmission electron microscopy, K. Briggman, S.K. Mikula and A. Scherbarth for help with staining procedures, B. Titze for help with conductive coating, J. Tritthardt for developing electronic circuits and M. Mueller for help with scanning electron microscopy-related software. We also thank the following student tracers: M. Diemer, C. Domnick, J. Hanne, P. Hofmann, A. Ivanova, H. Jakobi, A. Klein, J. Löffler, J. Nassel, J. Trendel and P. Weber. This work was supported by the Max Planck Society and the Deutsche Forschungsgemeinschaft (DFG).

AUTHOR CONTRIBUTIONS

S.M. and W.D. designed the study and devised the analysis; S.M. carried out the experiments; J.B. and W.D. devised the aberration correction algorithm; S.M. analyzed the data; and S.M. and W.D. wrote the paper.

COMPETING FINANCIAL INTERESTS

The authors declare competing financial interests: details are available in the [online version of the paper](#).

Published online at <http://www.nature.com/doi/10.1038/nmeth.2213>. Reprints and permissions information is available online at <http://www.nature.com/reprints/index.html>.

- Kasthuri, N. & Lichtman, J.W. *Nat. Methods* **4**, 307–308 (2007).
- Bohland, J.W. *et al. PLoS Comput. Biol.* **5**, e1000334 (2009).
- Tsai, P.S. *et al. J. Neurosci.* **29**, 14553–14570 (2009).
- Sabatini, D.D., Bensch, K. & Barnett, R.J. *J. Cell Biol.* **17**, 19–58 (1963).
- Dalton, A.J., Kahler, H., Striebich, M.J. & Lloyd, B. *J. Natl. Cancer Inst.* **11**, 439–461 (1950).
- Palay, S.L., McGee-Russell, S.M., Gordon, S. Jr. & Grillo, M.A. *J. Cell Biol.* **12**, 385–410 (1962).
- Seligman, A.M., Wasserkrug, H.L. & Hanker, J.S. *J. Cell Biol.* **30**, 424–432 (1966).
- Li, A. *et al. Science* **330**, 1404–1408 (2010).
- Chung, J.R. *et al. Front. Neuroinform.* **5**, 29 (2011).
- Dempster, W.T. *Am. J. Anat.* **107**, 59–72 (1960).
- Hagström, L. & Bahr, G.F. *Histochem. Cell Biol.* **2**, 1–4 (1960).
- Bozzola, J.J. & Russell, L.D. *Electron Microscopy: Principles and Techniques for Biologists*. (Jones & Bartlett Learning, 1999).
- Hayat, M.A. *Principles and Techniques of Electron Microscopy: Biological Applications*, 4th edn. (Cambridge University Press, 2000).
- Van Holde, K.E. *J. Phys. Chem.* **63**, 1574–1577 (1959).
- Bahr, G.F. *Exp. Cell Res.* **7**, 457–479 (1954).
- Guha, P.C. & De, S.C. *J. Chem. Soc. Trans.* **125**, 1215–1218 (1924).
- De Bruijn, W.C. in *Proc. 4th Eur. Reg. Conf. Electron Microsc.* (ed. Bocciarelli, D.S.) 11–65 (Rome: Tipografia Polyglotta Vaticana, 1968).
- Karnovsky, M.J. in *Proc. 11th Meet. Am. Soc. Cell Biol.* 146 (1971).
- Seligman, A.M., Hanker, J.S., Wasserkrug, H., Dmochowski, H. & Katzoff, L. *J. Histochem. Cytochem.* **13**, 629–639 (1965).
- Quarles, R.H., Macklin, W.B. & Morell, P. in *Basic Neurochemistry: Molecular, Cellular, and Medical Aspects*, 7th edn. (eds Siegel, G., Albers, R.W., Brady, S. & Price, D.) Ch. 4, 51–72 (Academic, 2006).
- Spurr, A.R. *J. Ultrastruct. Res.* **26**, 31–43 (1969).
- Kushida, H. *J. Electron Microsc.* (Tokyo) **23**, 197 (1974).
- Partadiredja, G., Miller, R. & Oorschot, D.E. *J. Neurocytol.* **32**, 1165–1179 (2003).
- Sturrock, R.R. *Neuropathol. Appl. Neurobiol.* **6**, 415–420 (1980).

ONLINE METHODS

Animals used. A total of 45 adult (10- to 36-week-old) wild-type (C57BL/6) male mice, maintained at a 12-h dark-light cycle under standard chow, were used. Out of these, three (10-week-old) mice were used for whole-brain block-face imaging and traceability analysis. The remaining animals were used for general staining-protocol testing and optimization.

Mice were anesthetized with isoflurane (Baxter) inhalation and killed by transcardially perfused fixative. One brain (WB1405) was used for acquiring whole-brain coronal block-face mosaics at 80-nm pixel size for the purpose of assessing staining and embedding quality and uniformity. The remaining two brains (WB1406 and WB1407) were used for extracting small (<1 mm³) regions of interest (ROIs) for SBEM imaging²⁵. All procedures were approved by the local animal care and use committee and were in accordance with the laws of animal experimentation issued by the German federal government.

Sample preparation. The optimized whole-brain staining protocol, wbPATCO, was performed as follows (the methods used for exploratory preparations^{7,19,26–29} are given in **Supplementary Table 1**). After anesthesia, the mouse was placed supine and a horizontal cut was made into the upper abdomen. First the diaphragm was cut, then the ribs were cut laterally and the chest flap was folded back using a hemostat. The heart was exposed and held in place using serrated curved forceps (Moria MC31, Fine Science Tools) while a 22-gauge cannula was carefully inserted into the left ventricle and secured using an aneurysm clamp (Fine Science Tools). The right auricle was pierced, and the mouse was perfused transcardially at a rate of 0.5 ml/s with 40 ml of a 0.418 M (10%) solution of acrolein³⁰ (Sigma) in 0.1 M sodium cacodylate buffer (Serva), pH-adjusted to 7.4 with HCl and chilled to 2 °C. We chose acrolein as the fixative because with glutaraldehyde, but not with acrolein, we occasionally saw artifacts in the form of densely stained spots inside the myelin sheath. The mouse was subsequently decapitated, the muscle and skin tissue around the cranium and the cervical vertebrae were removed with small scissors (Fine Science Tools), and, starting from the vertebrae and working rostrally, the vertebrae and small bone fragments were carefully removed using #2 forceps until the entire brain was exposed dorsally and laterally. During this procedure, a transfer pipet was periodically used to drop fixative solution onto the brain to prevent dehydration. The cranial nerves were cut with small scissors before we removed the brain and placed it into an acrolein solution for post-fixation (48 h at 2 °C) followed by five 8-h rinses with 50 ml of 0.1 M cacodylate buffer. Brains were then either used for whole-brain staining, hemispherectomized with a scalpel blade and used for hemisphere staining or diced into small cubes (<1 mm³) for small-sample staining.

For all immersion steps the samples were kept in closed centrifuge tubes (Sarstedt), which were discarded after each staining step. Small samples were incubated in 1 ml of staining solution for 90 min in 2-ml centrifuge tubes (Sarstedt) on a rotator. Rinse cycles consisted of three 10-min immersions in 2 ml of 0.1 M cacodylate, pH 7.4, at 20 °C. Embedding of small samples was performed as described below except that volumes were 2 ml and durations were 30 min each. Hemispheres were incubated in 12.5 ml of staining solution for 24 h in 15-ml centrifuge tubes during gentle agitation. Rinse cycles between successive staining steps

consisted of four 4-h immersions in 25 ml of 0.1 M cacodylate, pH 7.4, at 20 °C. Embedding of hemispheres was performed as described below except that volumes were 25 ml and durations were 6 h each. Whole brains were incubated in 25 ml of staining solution for 48 h in 50-ml centrifuge tubes during gentle agitation. Rinse cycles between successive staining steps consisted of four 8-h immersions in 50 ml of 0.1 M cacodylate, pH 7.4, at 20 °C.

For the wbPATCO stain, the whole brain was first placed into a solution containing 90 mM periodic acid (Sigma) in 0.1 M cacodylate buffer (Serva) at pH 7.4, at 2 °C for 48 h. It was then rinsed four times, immersed for 48 h in a solution of 100 mM TCH (Sigma) in 0.1 M cacodylate buffer at pH 7.4, held at 50 °C, rinsed four times and finally immersed for 48 h into a solution of 80 mM (2%) OsO₄ (Electron Microscopy Sciences) in water at 20 °C.

For embedding, brains were first dehydrated by immersing them sequentially for 12 h each in a series of acetone-water mixtures (50%, 75%, 100% and again 100% acetone) followed by epoxy-monomer infiltration by immersion (12 h, 25 ml each) into mixtures of acetone and epoxy resin (50%, 100% and 100% epoxy) with gentle agitation. All dehydration and infiltration steps were performed at 20 °C. Epoxy resins were either Spurr's²¹, using ERL-4221 as a replacement for ERL-4206, or Quetol²², and consisted of the following formulations: for Spurr's, 10 g ERL-4221 (Serva), 5 g DER 736 (Serva), 26 g NSA (Electron Microscopy Sciences) and 0.2 g DMAE (Serva); for Quetol, 10 g Quetol 651 (Electron Microscopy Sciences), 20 g NSA, 0.15 g DMAE. The brain was then placed into a custom-made rectangular silicone mold of dimensions 6 mm × 8.5 mm × 18 mm or 7 mm × 10 mm × 18 mm and cured at 70 °C for at least 24 h. We used Spurr's for embedding WB1406 and Quetol for WB1405 and WB1407.

Whole-brain block-face imaging. One sample (WB1405) was used for acquiring whole-brain coronal block-face mosaics at 80-nm pixel size to assess staining and ultrastructural preservation. Excess epoxy and the anterior portion of the brain were removed using an EM sample trimmer (EM Trim, Leica). The cross-sectional surface was then smoothed using an 8-mm-wide diamond knife (JumboHisto, Diatome) at a 3.5°-clearance-angle setting on the microtome, advances of 70–100 nm between cuts and 1.0 mm/s cutting speed. The smoothed block face was then coated with a 5-nm-thick layer of platinum-carbon using an electron-beam evaporator (MED 20, Bal-Tec) to allow charge dissipation during imaging.

The smoothed cross-sectional surface was not planar for two reasons. First, the sample moves in an arc on the ultramicrotome, which leads to a cylindrical shape; and second, the sample continues to shrink under vacuum slightly but unevenly after cutting and coating. This means the focus has to be corrected during mosaic acquisition. To provide approximately correct starting values for the autofocus algorithm used during the actual acquisition, we determined the correct working distance (WD) for all points lying on an evenly spaced (1-mm) grid by manual focusing, and we then interpolated between points with cubic splines. Next, we automatically acquired all tiles needed for the mosaic using a custom-written Matlab (MathWorks) script that controlled the scanning electron microscopy (SEM, Merlin, Zeiss) and the external scan generator (Atlas, Fibics/Zenith). Prior to the acquisition of each tile, the script, after determining which part of the tile had

the best contrast, called a custom aberration-correction procedure³¹ for both WD and astigmatism.

Images were acquired using 5.0-keV landing energy, 1-nA beam current, 2- μ s pixel dwell time and 6.0-mm WD. Secondary electrons were detected using the built-in Everhart-Thornley (ET) detector, with the grid voltage set to 400 V. To prevent secondary electrons from being drawn into the column, we inserted a custom aperture (diameter of 2 mm) into the end cap. The tile size was 4,000 \times 4,000 pixels, which results in a 330- μ m field-of-view. Substantially larger tiles could not be used without incurring a loss of resolution at the image corners. We used a 5% overlap between tiles, which was enough to calculate tile offsets with sub-pixel precision by cross-correlation. The offsets were then used in a global alignment and stitching procedure based on iteratively minimizing the weighted (by the reciprocal residuals) sum of the squared residual shifts^{32,33}. The data set comprised 975 tiles that were combined into a final mosaic 153,000 \times 98,000 pixels in size. All image processing was performed using custom Matlab code. The final mosaic is available for online viewing (<http://homes.mpg.de/~smikula/blockface/>) using a custom javascript/dHTML interface³⁴.

TEM imaging. Myelin-sheath and synaptic ultrastructure were assessed at high resolution by transmission electron microscopy (TEM). For this, a small cube from the dorsolateral striatum was dissected out from an embedded whole-brain sample with a scalpel blade and mounted on a metal stub. Then, 70-nm-thick sections were cut using an ultramicrotome (Ultracut, Leica), mounted on Formvar-coated copper TEM grids (Plano GmbH), post-stained in 2% (50 mM) aqueous uranyl acetate²⁶ and lead citrate³⁵ for 10 and 5 min each, respectively, and imaged on a transmission electron microscope (JEM 1400, JEOL) at 80-keV electron energy, with images recorded on a CCD camera.

Serial block-face imaging. For SBEM imaging, a total of eight ROIs were selected from WB1406 and WB1407. The random selection of a white- or gray-matter ROI was performed by generating pseudo-random 3-tuples until the bregma-referred coordinates corresponding to the 3-tuple pointed to, respectively, a white- or gray-matter location inside of the brain, as determined by consulting the Paxinos mouse atlas³⁶. This was repeated until coordinates for all ROIs were obtained. We then trimmed the sample coronally, starting from the anterior end of the brain to the approximate location of the most anterior ROI, smoothed and imaged the block face. Once the ROI had been located in the SEM using visual cues, it was repeatedly imaged with high beam current to mark the ROI on the block face. This mark was then used to visually identify the ROI in a dissecting scope, and a small volume of sample at the ROI was cut out with a scalpel blade, mounted on a stub and imaged with SBEM on a QuantaFEG 200 (FEI). The whole-brain sample was then retrimmed to the next ROI and the process was repeated. For each ROI, a data set of approximately (80 μ m)³ was acquired at 40-nm isotropic voxel size. SBEM imaging parameters were 2.8-keV primary beam electron energy, 155-pA beam current, 8- μ s pixel dwell time, 6.0-mm WD and 20-Pa water vapor pressure. Backscattered electrons were detected

using a custom silicon-diode detector (AXUV, International Radiation Detectors) combined with a custom current amplifier.

Traceability analysis. For axon traceability analysis, SBEM data sets (2,048 \times 1,768 \times 1,800 voxels), originally acquired at 40 nm, were also prepared as data sets down-sampled to 80 and 120 nm by selecting, respectively, every second or third voxel in *x*, *y* and *z*. Using a custom Matlab script, data sets were split into cubes (128 \times 128 \times 128 voxels) as needed for the Knossos software (www.knossos-tool.org/). Using Knossos, 50 axons were randomly chosen among those passing through the central region of the 40-nm-resolution data set. Each of those axons was independently traced by five undergraduate tracers at each resolution.

To quantify myelinated-axon traceability, tracing errors were detected by manually comparing each individual axon tracing to the 40-nm consensus tracing of the same axon. The consensus tracing was the largest subset of tracings (at least two) that, in both tracing directions, agreed with each other until they either reached the surface of the SBEM data set or a node of Ranvier located within 10 μ m of the nearest data set surface. The latter condition accounted mainly for cases in which a node of Ranvier extended beyond the data set. Because the unmyelinated stretch of axon at a node had low contrast, tracing relied heavily on finding the matching paranode. If no such node could be found or if no two tracers agreed on which paranode to select, the correct paranode was likely outside of the data set. Other possibilities are that the tracing had reached a terminal branch or the initial segment, both of which are unmyelinated.

Although it is theoretically possible to end up with two sets of two tracings for each axon that are consistent within but inconsistent between sets, this was never observed. Errors were classified by whether or not they occurred at nodes of Ranvier. Consensus tracings of collaterals were not included in the analysis because they were infrequent (3.5% of total tracings), occurring mainly in V1. We computed error rates per millimeter by dividing the total number of errors by the combined total path lengths for the respective axons, using the median path lengths of their respective 40 nm tracings. The axon diameter was computed using the mean of ten measurements randomly selected along the internodes of the axon.

25. Denk, W. & Horstmann, H. *PLoS Biol.* **2**, e329 (2004).

26. Terzakis, J.A. *J. Ultrastruct. Res.* **22**, 168–184 (1968).

27. Walton, J. *J. Histochem. Cytochem.* **27**, 1337–1342 (1979).

28. Willingham, M.C. & Rutherford, A.V. *J. Histochem. Cytochem.* **32**, 455–460 (1984).

29. Deerinck, T.J. *et al. Microsc. Microanal.* **16** (suppl. 2), 1138–1139 (2010).

30. Luft, J.H. *Anat. Rec.* **133**, 305 (1959).

31. Binding, J., Mikula, S. & Denk, W. *Microsc. Microanal.* (in the press).

32. Holland, P.W. & Welsch, R.E. *Commun. Stat. Theory Methods* **6**, 813–827 (1977).

33. Baumann, M. *et al. in Proc. 6th PIMS Ind. Problem Solving Workshop* (ed. Macki, J.) Ch. 1, 1–25 (PIMS, 2002).

34. Mikula, S., Trotts, I., Stone, J.M. & Jones, E.G. *Neuroimage* **35**, 9–15 (2007).

35. Reynolds, E.S. *J. Cell Biol.* **17**, 208–212 (1963).

36. Franklin, K.B.J. & Paxinos, G. *The Mouse Brain in Stereotaxic Coordinates* 3rd edn. (Academic, 2008).